

Bottom-up evolution of perovskite clusters into high-activity rhodium nanoparticles toward alkaline hydrogen evolution

Received: 8 April 2022

Accepted: 2 January 2023

Published online: 17 January 2023

Check for updates

Gaoxin Lin^{1,2,11}, Zhuang Zhang^{1,2,11}, Qiangjian Ju^{1,2,11}, Tong Wu^{1,2}, Carlo U. Segre³, Wei Chen⁴, Hongru Peng⁵, Hui Zhang⁶, Qiunan Liu⁷, Zhi Liu^{5,6}, Yifan Zhang^{1,2}, Shuyi Kong^{1,2}, Yuanlv Mao^{1,2}, Wei Zhao^{1,2}, Kazu Suenaga⁷, Fuqiang Huang^{1,8} ✉ & Jiacheng Wang^{1,2,9,10} ✉

Self-reconstruction has been considered an efficient means to prepare efficient electrocatalysts in various energy transformation process for bond activation and breaking. However, developing nano-sized electrocatalysts through complete in-situ reconstruction with improved activity remains challenging. Herein, we report a bottom-up evolution route of electrochemically reducing Cs₃Rh₂I₉ halide-perovskite clusters on N-doped carbon to prepare ultrafine Rh nanoparticles (~2.2 nm) with large lattice spacings and grain boundaries. Various in-situ and ex-situ characterizations including electrochemical quartz crystal microbalance experiments elucidate the Cs and I extraction and Rh reduction during the electrochemical reduction. These Rh nanoparticles from Cs₃Rh₂I₉ clusters show significantly enhanced mass and area activity toward hydrogen evolution reaction in both alkaline and chlor-alkali electrolyte, superior to liquid-reduced Rh nanoparticles as well as bulk Cs₃Rh₂I₉-derived Rh via top-down electro-reduction transformation. Theoretical calculations demonstrate water activation could be boosted on Cs₃Rh₂I₉ clusters-derived Rh nanoparticles enriched with multiply sites, thus smoothing alkaline hydrogen evolution.

Hydrogen, as an energy carrier, is critical to utilize the renewable energy including wind, solar and hydropower for sustainable development^{1–6}. The alkaline hydrogen evolution reaction (HER) with sluggish kinetics limits the efficiency of H₂ generation in water

electrolysis and chlor-alkali electrolysis due to the additional step of water dissociation^{7–12}. It starts from the cleaving of the H–OH bond coupled with an electron to form the adsorbed hydrogen atom (H_{ad}, Volmer step). Then, H₂ is produced by the combination of two

¹State Key Lab of High Performance Ceramics and Superfine microstructure, Shanghai Institute of Ceramics, Chinese Academy of Sciences, 201899 Shanghai, China. ²Center of Materials Science and Optoelectronics Engineering, University of Chinese Academy of Sciences, 100049 Beijing, China. ³Department of Physics & Center for Synchrotron Radiation Research and Instrumentation, Illinois Institute of Technology, Chicago, IL 60616, USA. ⁴Department of Mechanical, Materials and Aerospace Engineering, Illinois Institute of Technology, Chicago, IL 60616, USA. ⁵School of Physical Science and Technology, ShanghaiTech University, 201210 Shanghai, China. ⁶State Key Laboratory of Functional Materials for Informatics, Shanghai Institute of Microsystem and Information Technology, Chinese Academy of Sciences, 200050 Shanghai, China. ⁷SANKEN, Osaka University, Ibaraki 567-0047, Japan. ⁸State Key Laboratory of Rare Earth Materials Chemistry and Applications, College of Chemistry and Molecular Engineering, Peking University, 100871 Beijing, China. ⁹Hebei Provincial Key Laboratory of Inorganic Nonmetallic Materials, College of Materials Science and Engineering, North China University of Science and Technology, 063210 Tangshan, China. ¹⁰School of Materials Science and Engineering, Taizhou University, 318000 Taizhou, Zhejiang, China. ¹¹These authors contributed equally: Gaoxin Lin, Zhuang Zhang, Qiangjian Ju. ✉ e-mail: huangfq@mail.sic.ac.cn; jiacheng.wang@mail.sic.ac.cn

H_{ad} (Tafel step) or the interaction of H_{ad} and a water molecule (Heyrovsky step)^{7,13–15}. Thus, the properties of water dissociation, and hydroxy radical and hydrogen adsorption are crucial for alkaline HER.

To achieve high activity toward these basic steps in alkaline HER, it is necessary to design a functional composite with multiple active centers to facilitate the overall reaction^{16–21}. However, such a comprehensive system not only brings difficulty in material synthesis, but also is harmful to the durability of the catalyst due to element or phase segregation^{22–26}, especially in a harsh chlor-alkali solution. The potential-driven structural reconstruction of a pre-catalyst during the working conditions is an efficient method to enhance the electrochemical performance^{26–29}. The reconstruction of pre-catalysts could obtain the amorphous or defect-rich structure, increased accessible surface area, optimized adsorption properties, and promoted charge transfer^{30–33}, thus leading to the improvement of activity and stability. For example, Ni_2P could be transformed in situ into Ni_2P/NiO_x core-shell structure during oxygen evolution reaction³⁴. It could accelerate water adsorption and dissociation kinetics due to unique heterostructures and multiple active centers. Besides, the $SrIrO_3$ perovskite electrode experiences self-reconstruction during the alkaline HER because of lattice Sr^{2+} leaching³⁵. The formed metallic Ir on the surface of perovskite results in the remarkable activity enhancement as well as excellent stability. However, most pre-catalysts undergo the surface-reconstruction, which leads to the low component utilization as the inert internal part is inaccessible to the surface catalysis. Moreover, the reconstruction degree is highly relevant to the reaction environment, and it may be changed with pH, temperature, electrolyte, and applied potential^{31,36–38}, which is disadvantageous to the industrial extreme condition. Therefore, the electrocatalysts consisting of

single-component nanoparticles prepared via complete in situ reconstruction are highly desired to avoid the above problems during the alkaline HER.

Herein, we develop a bottom-up evolution route to prepare high-activity Rh nanoparticles via in situ electrochemical reduction of new $Cs_3Rh_2I_9$ perovskite clusters. These electrochemically reduced Rh nanoparticles could be used as a highly efficient HER catalyst in both alkaline and chlor-alkali electrolyte. The new halide-perovskite compound $Cs_3Rh_2I_9$ with dimer unit $[Rh_2I_9]^{3-}$ separated by Cs ions as the pre-catalyst of electrochemically synthesized Rh nanoparticles was synthesized by solid state reaction (Fig. 1a). It could be dissolved in N, N-dimethylformamide (DMF). The unique zero-dimensional structure allows it to be downsized into small clusters on a polar nitrogen-doped carbon (NC) support by a simple dissolution-precipitation method (Fig. 1b). The high surface energy of $Cs_3Rh_2I_9$ clusters on NC ($Cs_3Rh_2I_9/NC$) could promote an electrochemical self-reduction and bottom-up evolution, leading to the formation of unique Rh nanoparticles with larger lattice spacings and lower atomic coordination number (Fig. 1b). In sharp contrast, such Rh nanoparticles cannot be formed from bulk $Cs_3Rh_2I_9$ and liquid reduction of $RhCl_3$ by $NaBH_4$ (Fig. 1c, d). The complete reconstructed $Cs_3Rh_2I_9/NC-R$ could significantly reduce the barrier of water dissociation in alkaline HER. Therefore, $Cs_3Rh_2I_9/NC-R$ exhibits high mass activity of $772.1 \text{ mA mg}^{-1}_{Rh}$ in a chlorine-alkali electrolyte, which is about 2.5 times and 35.5 times that of liquid-reduced Rh/NC with similar particle size and electrochemically reduced $Cs_3Rh_2I_9-R$ with the larger size, respectively (Fig. 1e, f). And it also shows the negligible activity loss after 50 h durable measurement.

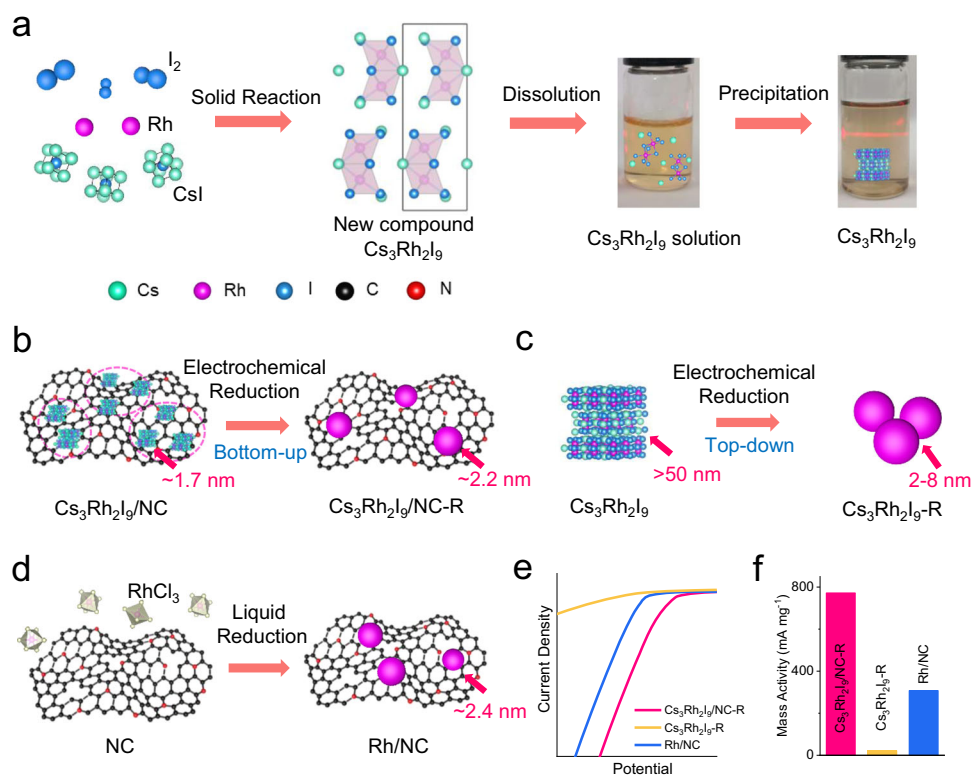


Fig. 1 | Schematic illustration of synthesizing perovskite $Cs_3Rh_2I_9$ bulk crystals and clusters $Cs_3Rh_2I_9/NC$, and their electrochemical reduction into metallic Rh particles toward alkaline HER. a Synthesis of $Cs_3Rh_2I_9$ bulk crystal via a solid reaction using I_2 , Rh, and CsI at $800^\circ C$. The $Cs_3Rh_2I_9$ crystal could demonstrate a dissolution-precipitation phenomenon in N, N-dimethylformamide (DMF). **b** Electrochemical reduction of $Cs_3Rh_2I_9$ clusters ($\sim 1.7 \text{ nm}$) supported on NC ($Cs_3Rh_2I_9/NC$) to form $Cs_3Rh_2I_9/NC-R$ with a little larger size ($\sim 2.2 \text{ nm}$) via a bottom-

up evolution route. **c** Electrochemical reduction of bulk $Cs_3Rh_2I_9$ to form $Cs_3Rh_2I_9-R$ with very large particle size via a top-down route. **d** Liquid reduction of $RhCl_3$ in aqueous solution to form Rh/NC with average particle size of 2.4 nm as the control catalyst. **e** HER polarization curves of $Cs_3Rh_2I_9/NC-R$, $Cs_3Rh_2I_9-R$, and Rh/NC coated on rotating glassy carbon electrode (GCE, 1600 rpm) in a chlorine-alkali electrolyte. **f** HER mass activity comparison in a chlorine-alkali electrolyte for $Cs_3Rh_2I_9/NC-R$, $Cs_3Rh_2I_9-R$, and Rh/NC electrocatalysts at an overpotential of 50 mV .

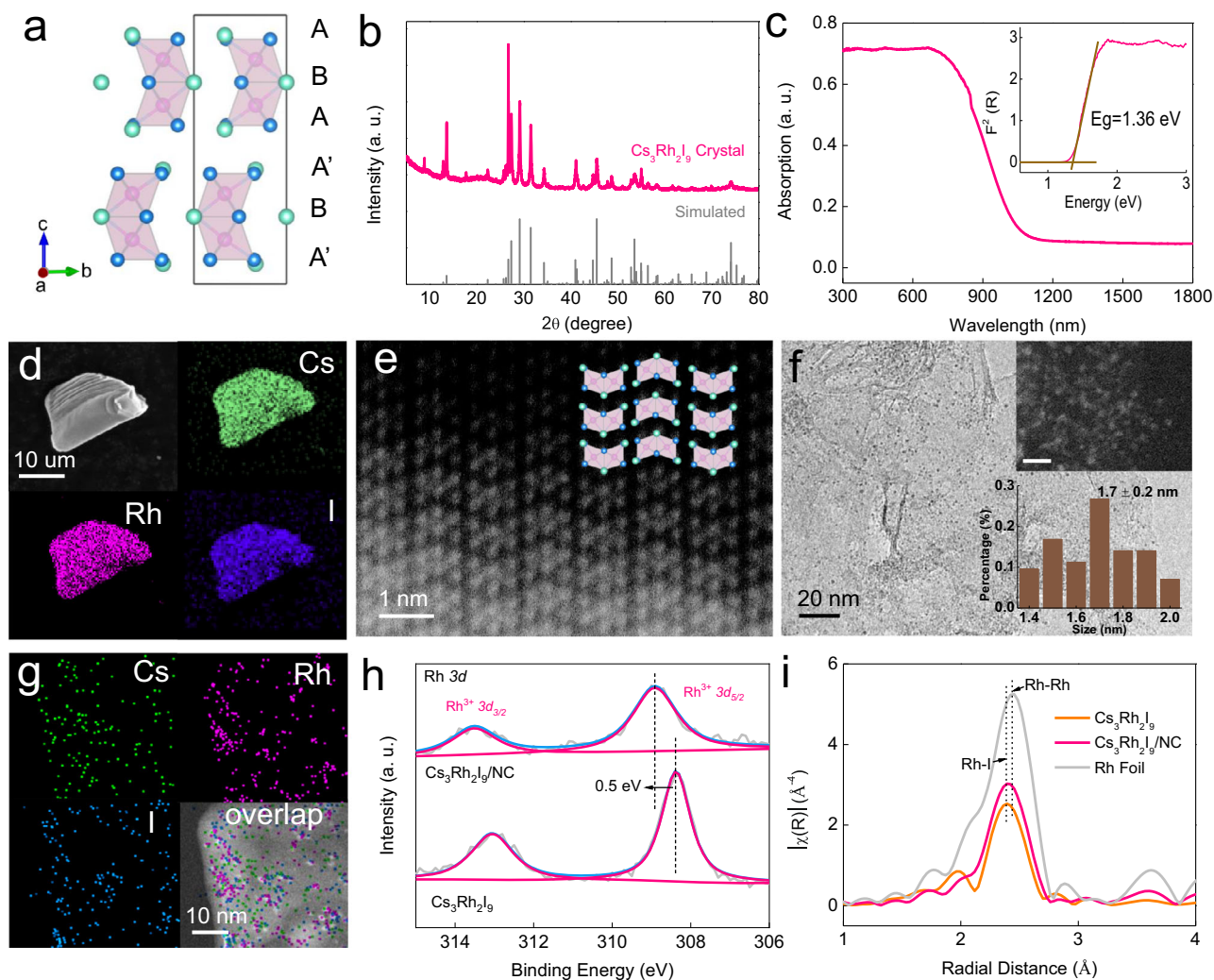


Fig. 2 | Structure characterization of bulk $\text{Cs}_3\text{Rh}_2\text{I}_9$ and nanoclusters $\text{Cs}_3\text{Rh}_2\text{I}_9/\text{NC}$. **a** Atomic structure, and **(b)** powder XRD pattern and simulated pattern of $\text{Cs}_3\text{Rh}_2\text{I}_9$ crystal. **c** Diffuse-reflectance UV-Vis spectrum of $\text{Cs}_3\text{Rh}_2\text{I}_9$. The inset shows the corresponding Tauc plot. **d** SEM-EDX mapping images of $\text{Cs}_3\text{Rh}_2\text{I}_9$ single crystal. **e** HAADF-STEM image of $\text{Cs}_3\text{Rh}_2\text{I}_9$ crystal. **f** TEM image of $\text{Cs}_3\text{Rh}_2\text{I}_9$ clusters

supported on NC ($\text{Cs}_3\text{Rh}_2\text{I}_9/\text{NC}$, Rh content: 5.8 wt.%). The insets show the corresponding HAADF image (scale bar: 5 nm, up) and particle size distribution (down). **g** TEM-EDX mapping of $\text{Cs}_3\text{Rh}_2\text{I}_9/\text{NC}$. **h** XPS spectra of Rh 3d for $\text{Cs}_3\text{Rh}_2\text{I}_9$ and $\text{Cs}_3\text{Rh}_2\text{I}_9/\text{NC}$. **i** Fourier transform EXAFS of Rh K-edge in R-space for $\text{Cs}_3\text{Rh}_2\text{I}_9$, $\text{Cs}_3\text{Rh}_2\text{I}_9/\text{NC}$, and Rh foil.

Results

Synthesis and characterization of bulk and cluster $\text{Cs}_3\text{Rh}_2\text{I}_9$

As a new compound, $\text{Cs}_3\text{Rh}_2\text{I}_9$ single crystals were synthesized by the solid state reaction using CsI as the flux. Its structure was determined by single-crystal X-ray diffraction (XRD). It belongs to the hexagonal $P6_3/mmc$ space group with $a = b = 7.9648$ (14) Å, $c = 20.028$ (4) Å, $V = 1100.3$ (4) Å³, $Z = 2$, and a calculated density of $d = 5.272$ g cm⁻³. Details of the atomic coordinates in the compound are shown in Supplementary Table 1, 2. $\text{Cs}_3\text{Rh}_2\text{I}_9$ with a zero-dimensional structure consists of alternating hexagonal CsI_3 layers in ABA'BA' stacking sequence (Fig. 2a). Two adjacent $[\text{RhI}_6]^{3-}$ octahedrons share three I atoms on the plane B to form a $[\text{Rh}_2\text{I}_9]^{3-}$ dimer. The powder XRD pattern of $\text{Cs}_3\text{Rh}_2\text{I}_9$ is consistent with the simulated result (Fig. 2b), confirming its zero-dimensional perovskite structure³⁹. $\text{Cs}_3\text{Rh}_2\text{I}_9$ shows a semiconductor behavior with an optical band gap of 1.36 eV (Fig. 2c)⁴⁰. Single-crystal $\text{Cs}_3\text{Rh}_2\text{I}_9$ is diamagnetic due to the d^6 electronic configuration of Rh^{3+} (Supplementary Fig. 2). Energy dispersive X-ray (EDX) spectroscopy shows homogenous distribution of Cs, Rh, and I elements in crystalline $\text{Cs}_3\text{Rh}_2\text{I}_9$ (Fig. 2d) and EDX results from TEM show Cs, Rh and I with an atomic ratio of ~3:2:9, consistent with the stoichiometry of $\text{Cs}_3\text{Rh}_2\text{I}_9$ (Supplementary Fig. 3 and Table 3).

The high-angle annular dark-field scanning transmission electron microscopy (HAADF-STEM) confirms the alternating CsI_3 layer structure (Fig. 2e). $\text{Cs}_3\text{Rh}_2\text{I}_9$ also exhibits good stability as its structure does not change in 1.0 M HCl or KOH for 7 days (Supplementary Fig. 5).

$\text{Cs}_3\text{Rh}_2\text{I}_9$ can be dissolved in N, N-dimethylformamide (DMF) to form a brownish yellow solution due to the polar aprotic property of DMF (Supplementary Fig. 6). When adding water, $\text{Cs}_3\text{Rh}_2\text{I}_9$ precipitates without any change of structure (Supplementary Fig. 7, 8 and 10). By this means, the use of polar nitrogen-doped carbon (NC) during the precipitation process can significantly reduce the particle size to form $\text{Cs}_3\text{Rh}_2\text{I}_9$ nanoclusters on NC ($\text{Cs}_3\text{Rh}_2\text{I}_9/\text{NC}$). Figure 2f shows the uniform distribution of $\text{Cs}_3\text{Rh}_2\text{I}_9$ nanoclusters with a size of ~1.7 nm. No obvious particles were observed in SEM images, further confirming the uniform and ultra-small size of $\text{Cs}_3\text{Rh}_2\text{I}_9$ (Supplementary Fig. 9). The structure and composition of $\text{Cs}_3\text{Rh}_2\text{I}_9/\text{NC}$ is the same as $\text{Cs}_3\text{Rh}_2\text{I}_9$ (Fig. 2g and Supplementary Fig. 10). The X-ray photoelectron spectroscopy (XPS) spectra show a positive core level shift of about 0.5 eV for $\text{Cs}_3\text{Rh}_2\text{I}_9/\text{NC}$ (Fig. 2h), indicating the strong carrier effect of $\text{Cs}_3\text{Rh}_2\text{I}_9$ clusters on the NC⁴¹. The Rh-I coordination was identified by extended X-ray absorption fine structure (EXAFS; Fig. 2i). The shell at 2.40 Å represents the Rh-I scattering path for $\text{Cs}_3\text{Rh}_2\text{I}_9$ and

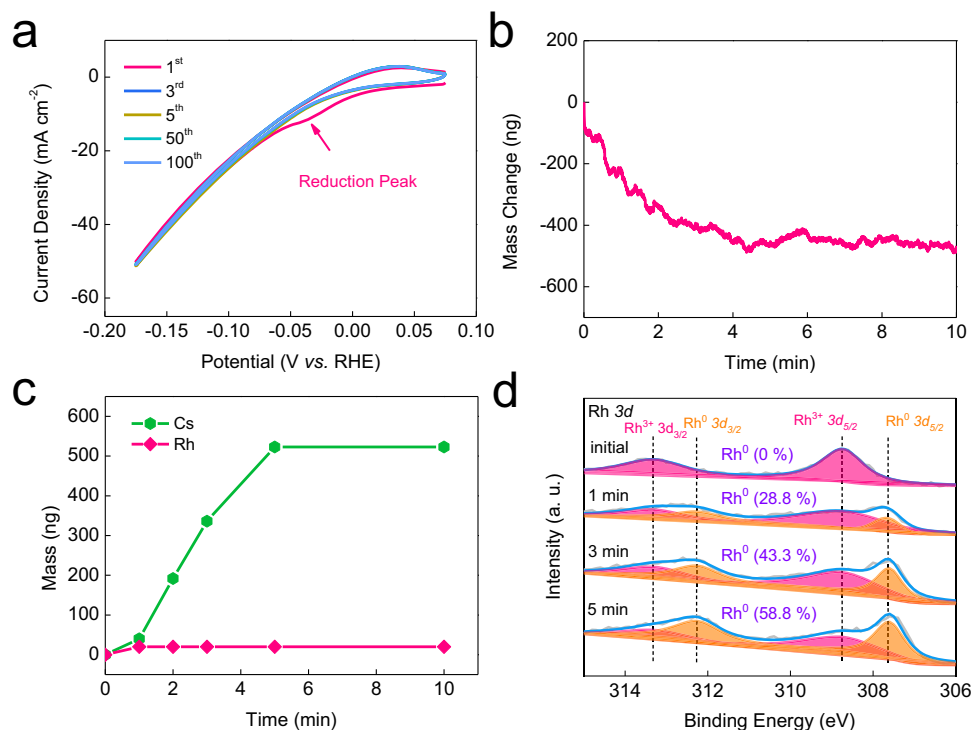


Fig. 3 | Reconstruction of clusters $\text{Cs}_3\text{Rh}_2\text{I}_9/\text{NC}$ into Rh nanoparticles on NC. **a** The CV curves from 1st to 100th cycle at 100 mV s⁻¹ for $\text{Cs}_3\text{Rh}_2\text{I}_9/\text{NC}$ in 1.0 M KOH. **b** Mass change of the $\text{Cs}_3\text{Rh}_2\text{I}_9/\text{NC}$ electrode monitored by in situ EQCM experiment. **c** ICP-MS of the Cs and Rh contents in the electrolyte at different

reduction time. **d** XPS spectra of Rh 3d for $\text{Cs}_3\text{Rh}_2\text{I}_9/\text{NC}$ at different reduction time. The results in (b–d) were obtained at the potentiostatic measurement at -0.03 V vs. RHE.

$\text{Cs}_3\text{Rh}_2\text{I}_9/\text{NC}$, while the fitting results suggest that an additional Rh–Rh scattering path appears in $\text{Cs}_3\text{Rh}_2\text{I}_9/\text{NC}$ (Supplementary Fig. 13 and Table 4). This may be caused by partial decomposition of $\text{Cs}_3\text{Rh}_2\text{I}_9$ nanoclusters under the high-energy measurement (Supplementary Fig. 14).

Electrochemical reduction of $\text{Cs}_3\text{Rh}_2\text{I}_9$

Under cathodic potentials, it was found that both $\text{Cs}_3\text{Rh}_2\text{I}_9$ clusters and single crystals are unstable and could be transformed into Rh particles. Especially, the $\text{Cs}_3\text{Rh}_2\text{I}_9$ nanoclusters on NC can be electrochemically reduced and assembled into Rh nanoparticles with mean particle size of 2.2 nm via a bottom-up evolution route (Fig. 1b). The reduction peak at about -0.035 V versus reversible hydrogen electrode (vs. RHE) in the first CV curve corresponds to the reduction of Rh^{3+} (Fig. 3a). The in situ Raman experiments indicate that the characteristic structure of $\text{Cs}_3\text{Rh}_2\text{I}_9$ disappears when the negative potential was applied (Supplementary Fig. 15). To elucidate the process of reconstruction, the reduction was conducted by the potentiostatic measurement at -0.03 V vs. RHE. The in situ electrochemical Quartz Crystal Microbalance (EQCM) experiment indicates that the quality of the electrode continuously decreases and then stabilizes after about 5 min (Fig. 3b). The Inductively Coupled Plasma Mass Spectrometry (ICP-MS) results show the content of Cs^+ ions in the electrolyte continuously increases in the initial 5 min while Rh in the electrolyte was barely detected (Fig. 3c). And the XPS spectra shows neither Cs nor I was detected after reduction (Supplementary Fig. 16), which is also confirmed by ICP-MS results (Supplementary Table 5). Rh mass content in $\text{Cs}_3\text{Rh}_2\text{I}_9/\text{NC-R}$ was determined by the ICP-MS to be 5.7 ± 0.8 wt.%, which is very close to the initial loading of 5.8 wt.%. This indicates all $\text{Cs}_3\text{Rh}_2\text{I}_9$ nanoclusters could be electrochemically reduced to metallic Rh^0 nanoparticles. And such a reconstruction process is complete. The ex-situ XPS spectra verify the content of Rh^{3+} decreases while the content of Rh^0 increases with the reduction time (Fig. 3d and Supplementary Fig. 17).

TEM measurements confirm the uniform distribution of Rh particles on the NC after electrochemical reduction ($\text{Cs}_3\text{Rh}_2\text{I}_9/\text{NC-R}$, Fig. 4a and Supplementary Fig. 18) and the Rh particle size (~ 2.2 nm) is evidently larger than that of $\text{Cs}_3\text{Rh}_2\text{I}_9$ nanoclusters (~ 1.7 nm), implying a bottom-up evolution route under cathodic potential. The linear electron energy loss spectroscopy analysis suggests the element in the particle is Rh (Fig. 4b). The bulk $\text{Cs}_3\text{Rh}_2\text{I}_9$ can also be reconstructed in this way, but it does not reach a stable state within 300 CV cycles due its large size (Supplementary Fig. 19). After reduction ($\text{Cs}_3\text{Rh}_2\text{I}_9\text{-R}$), its edge consists of numerous Rh particles with larger size (4.3 ± 1.2 nm) compared to the product from $\text{Cs}_3\text{Rh}_2\text{I}_9/\text{NC}$ (Supplementary Fig. 20, 21). The Rh K-edge X-ray absorption near edge structure spectra indicates the adsorption edge of the reduced $\text{Cs}_3\text{Rh}_2\text{I}_9/\text{NC}$ ($\text{Cs}_3\text{Rh}_2\text{I}_9/\text{NC-R}$) shifts to lower energy compared to the initial state (Supplementary Fig. 22). Meanwhile, the shell in EXAFS for the $\text{Cs}_3\text{Rh}_2\text{I}_9/\text{NC-R}$ shifts to 2.45 Å (Fig. 4c), similar to that of Rh foil. The fitting results show that its Rh–Rh coordination number is only 8.0 (Fig. 4c and Supplementary Table 6), showing the small particle size. The wavelet transform (WT)-EXAFS analysis shows the first shell of $\text{Cs}_3\text{Rh}_2\text{I}_9/\text{NC-R}$ domain at $R = 2.45$ Å and $k = 9.90$ Å⁻¹ (Fig. 4d), similar to the Rh foil ($R = 2.43$ Å and $k = 9.80$ Å⁻¹) and different from $\text{Cs}_3\text{Rh}_2\text{I}_9/\text{NC}$ with Rh–Rh scattering path ($R = 2.40$ Å and $k = 9.50$ Å⁻¹).

Moreover, the HAADF-STEM images indicate the Rh nanoparticles in $\text{Cs}_3\text{Rh}_2\text{I}_9/\text{NC-R}$ are rich with grain boundaries (GBs) and large lattice spacings (0.225–0.230 nm) (Fig. 4e and Supplementary Fig. 24). In sharp contrast, the particles in electrochemically reduced $\text{Cs}_3\text{Rh}_2\text{I}_9$ ($\text{Cs}_3\text{Rh}_2\text{I}_9\text{-R}$) form bulk $\text{Cs}_3\text{Rh}_2\text{I}_9$ show smaller plane spacings of 0.220 nm and no evident GBs could be observed (Fig. 4f and Supplementary Fig. 21). The formation of twinned Rh with large lattice spacings in $\text{Cs}_3\text{Rh}_2\text{I}_9/\text{NC-R}$ may be ascribed to the coupling of smaller Rh clusters with high surface energy during the electrochemical reduction process. Limited by the size of the $\text{Cs}_3\text{Rh}_2\text{I}_9$ cluster (~ 1.7 nm), the formed Rh clusters could combine with neighboring clusters into

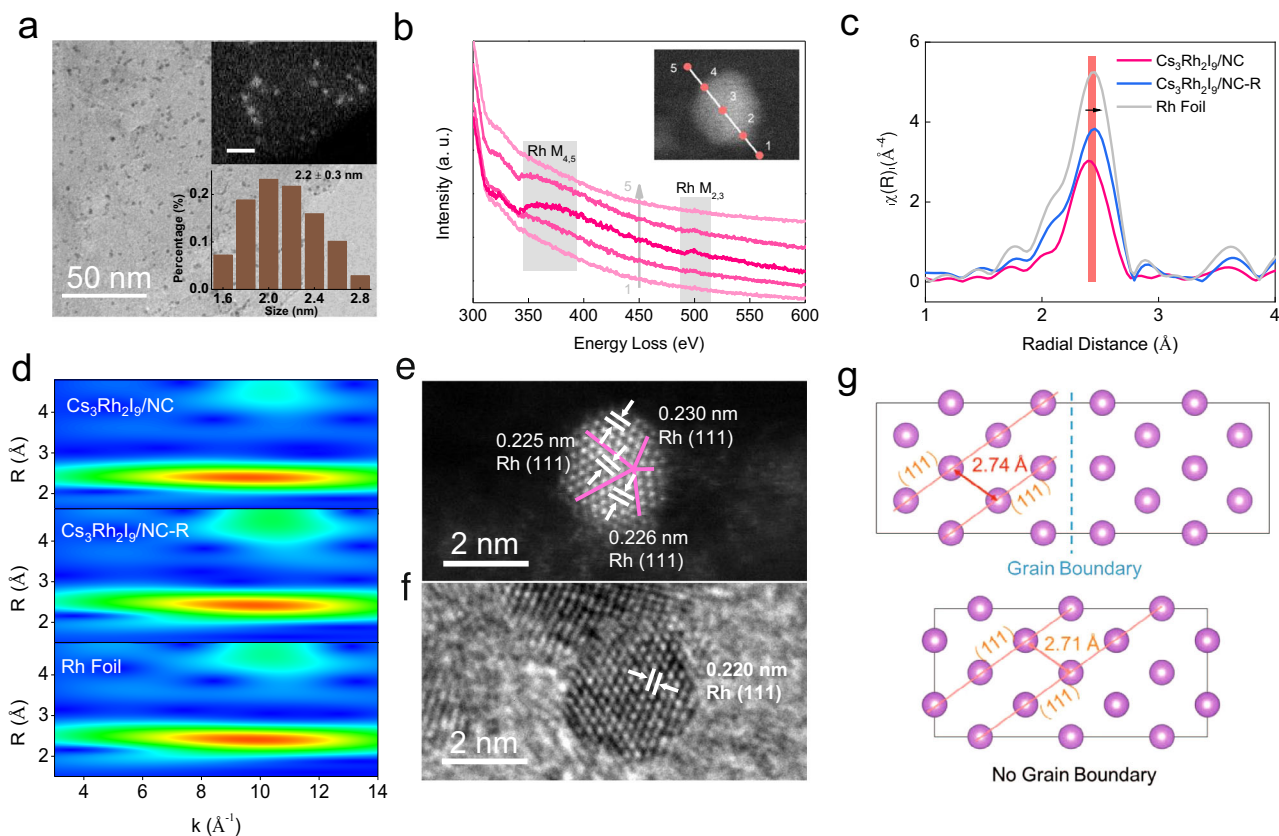


Fig. 4 | Characterization of $\text{Cs}_3\text{Rh}_2\text{I}_9/\text{NC-R}$ prepared by electrochemical reduction of $\text{Cs}_3\text{Rh}_2\text{I}_9/\text{NC}$. **a** TEM image of $\text{Cs}_3\text{Rh}_2\text{I}_9/\text{NC-R}$, showing uniform dispersion of Rh nanoparticles. The inset shows the corresponding HAADF image (scale bar: 5 nm, up) and particle size distribution (down). **b** The linear electron energy loss spectroscopy of $\text{Cs}_3\text{Rh}_2\text{I}_9/\text{NC-R}$. **c** Fourier transform EXAFS of the Rh K-edge in R-space for $\text{Cs}_3\text{Rh}_2\text{I}_9/\text{NC}$, $\text{Cs}_3\text{Rh}_2\text{I}_9/\text{NC-R}$ and Rh foil. **d** WT-EXAFS images

of Rh for $\text{Cs}_3\text{Rh}_2\text{I}_9/\text{NC}$, $\text{Cs}_3\text{Rh}_2\text{I}_9/\text{NC-R}$ and Rh foil. **e** HAADF-STEM image of $\text{Cs}_3\text{Rh}_2\text{I}_9/\text{NC-R}$, showing a single Rh nanoparticle with larger lattice spacing and twin-GBs. **f** HRTEM image of Rh nanoparticles ($\text{Cs}_3\text{Rh}_2\text{I}_9/\text{R}$) derived from the top-down electrochemical reduction of bulk $\text{Cs}_3\text{Rh}_2\text{I}_9$ crystal. **g** DFT models of Rh with larger lattice spacing and GBs (up panel) and Rh with regular lattice spacing (down panel).

particles (~ 2.2 nm) to decrease the surface energy (Supplementary Fig. 25). However, the Rh particles formed from bulk $\text{Cs}_3\text{Rh}_2\text{I}_9$ undergo a top-down process of bulk decomposition. They have particle sizes greater than 2 nm and thus are energetically stable enough to not combine into twin crystals. Furthermore, the twinned Rh in $\text{Cs}_3\text{Rh}_2\text{I}_9/\text{NC-R}$ exhibits tensile stress with the enlarged lattice fringe of 0.5–5.5% (Fig. 4e, Supplementary Fig. 24). The corresponding GB was established by density functional theory (DFT) calculation (Fig. 4g) to promote tensile stress of the nearby Rh atoms (from 2.71 to 2.74 Å), suggesting the rich GBs in twinned Rh can stabilize the enlarged (111) lattice. The Rh particle with such tensile stress is considered to facilitate H_2O dissociation in alkaline HER².

HER activity evaluation

The HER activity was first evaluated in 1.0 M KOH electrolyte. Before measurement, the electrode was in situ reduced under the CV between 0.075 and -0.175 vs. RHE at a scan rate of 100 mV s^{-1} to achieve a stable stage. The Rh/NC with mean size of ~ 2.4 nm was synthesized by liquid chemical reduction for comparison (Supplementary Fig. 26). The Rh mass content in Rh/NC is 7 wt.%, and the HRTEM implies the lattice spacing of Rh particle is 0.220 nm, similar to that of $\text{Cs}_3\text{Rh}_2\text{I}_9/\text{R}$ without tensile stress. As shown in Fig. 5a, the overpotential at 10 mA cm^{-2} for $\text{Cs}_3\text{Rh}_2\text{I}_9/\text{NC-R}$ composed of Rh twin nanoparticles is only 25 mV, evidently lower than those of $\text{Cs}_3\text{Rh}_2\text{I}_9/\text{R}$ (123 mV), Pt/C (32 mV) and Rh/NC (41 mV). Moreover, the Tafel slope (30.3 mV dec^{-1}) of $\text{Cs}_3\text{Rh}_2\text{I}_9/\text{NC-R}$ is also smaller than that of chemically reduced Rh/NC without GBs and tensile stress (34.8 mV dec^{-1}) (Supplementary Fig. 28a). It implies that the GBs and tensile stress in Rh nanoparticles have a

significant effect on boosting alkaline HER. Besides, $\text{Cs}_3\text{Rh}_2\text{I}_9/\text{NC-R}$ exhibits high mass activity of 839.8 $\text{mA mg}^{-1}_{\text{Rh}}$, 21.6 times that of $\text{Cs}_3\text{Rh}_2\text{I}_9/\text{R}$ and 2.4 times that of Rh/NC (Supplementary Fig. 28b). The mass loading of $\text{Cs}_3\text{Rh}_2\text{I}_9/\text{NC}$ s was also optimized and compared (Supplementary Fig. 29). The electrochemical surface area (ECSA) is enhanced with the increased mass loading, but the optimal activity is achieved at a Rh mass loading of 5.8 wt.% ($\text{Cs}_3\text{Rh}_2\text{I}_9/\text{NC-R}$; Supplementary Fig. 30–32). In addition, the H_2 production faradaic efficiency for twinned Rh ($\text{Cs}_3\text{Rh}_2\text{I}_9/\text{NC-R}$) was confirmed to be nearly 100% through a drainage method (Supplementary Fig. 33). The HER activity of $\text{Cs}_3\text{Rh}_2\text{I}_9/\text{NC-R}$ outperforms most of reported Rh-based electrocatalysts (Fig. 5b) and other advanced alkaline electrocatalysts (Supplementary Table 7).

The HER activity in the simulated chlorine-alkali electrolyte (3.0 M NaOH + 3.0 M NaCl) was further evaluated in a three-electrode system. As shown in Fig. 5c, the overpotentials for $\text{Cs}_3\text{Rh}_2\text{I}_9/\text{NC-R}$ are 21, 65, and 107 mV to reach current densities of 10, 50, and 100 mA cm^{-2} , respectively, significantly lower than those of $\text{Cs}_3\text{Rh}_2\text{I}_9/\text{R}$, Pt/C, and Rh/NC. The mass activity of $\text{Cs}_3\text{Rh}_2\text{I}_9/\text{NC-R}$ is 772.1 $\text{mA mg}^{-1}_{\text{Rh}}$ at -50 mV vs. RHE, outperforming $\text{Cs}_3\text{Rh}_2\text{I}_9/\text{R}$ (21.7 $\text{mA mg}^{-1}_{\text{Rh}}$) and Rh/NC (307.8 $\text{mA mg}^{-1}_{\text{Rh}}$) (Fig. 5d, e). The area activity normalized by ECSA of $\text{Cs}_3\text{Rh}_2\text{I}_9/\text{NC-R}$ is 0.067 mA cm^{-2} , manifesting a factor of 2.0 increase than that of Rh/NC (Fig. 5e and Supplementary Fig. 35b). These results confirm the excellent intrinsic activity of $\text{Cs}_3\text{Rh}_2\text{I}_9/\text{NC-R}$ enriched with defects. The enhanced activity may be ascribed to the reconstruction process. $\text{Cs}_3\text{Rh}_2\text{I}_9/\text{NC-R}$ with unsaturated atom coordination and more accessible area could accelerate water adsorption and dissociation processes, thus leading to the better performance. Furthermore,

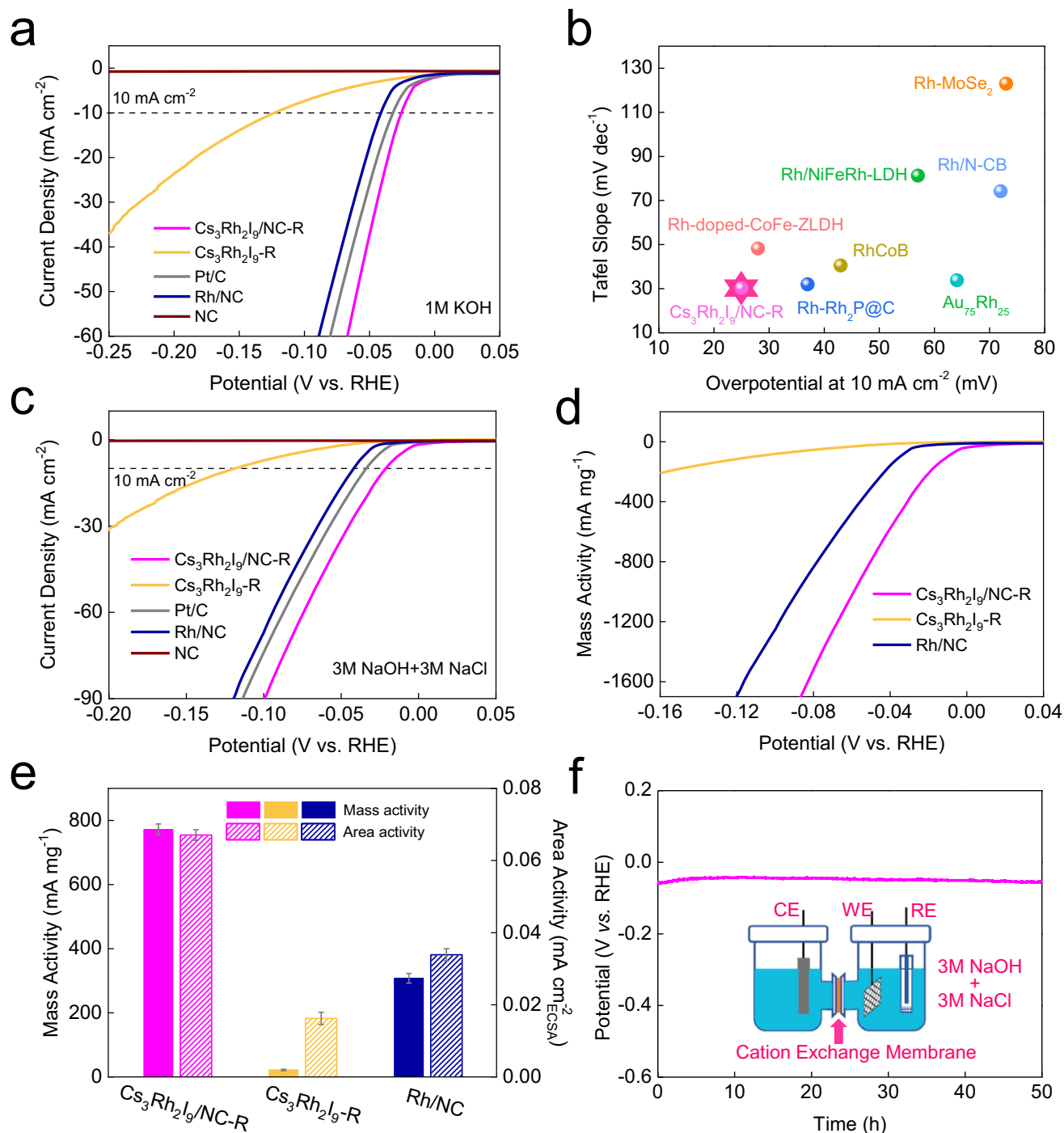


Fig. 5 | HER activity in 1.0 M KOH and chlor-alkali electrolyte. a LSV curves of various electrocatalysts including commercial Pt/C (Pt content: 20 wt.%) coated on rotating glassy carbon electrode (GCE, 1600 rpm) in 1.0 M KOH. The catalyst loading amount on GCE is 0.764 mg cm⁻². For Rh-based samples, the calculated Rh loading amounts on GCE are 0.045, 0.090 and 0.053 mg cm⁻² for Cs₃Rh₂I₉/NC-R, Cs₃Rh₂I₉-R, and Rh/NC, respectively. **b** Comparison of overpotential at 10 mA cm⁻² and Tafel slope for various Rh-based catalysts in 1.0 M KOH. **c** LSV curves of various

electrocatalysts coated on rotating GCE (1600 rpm) in chlorine-alkali electrolyte. **d** Mass activity normalized to the mass of Rh in chlorine-alkali electrolyte.

e Comparison of mass activity and area activity at the overpotential of 50 mV in chlorine-alkali electrolyte. All data show the mean and standard deviation through three repeated measurements. **f** Stability of Cs₃Rh₂I₉/NC-R at 10 mA cm⁻² in a chlorine-alkali electrolyte.

Cs₃Rh₂I₉/NC-R exhibits good durability with negligible activity loss after 50 h (Fig. 5f). After the durability measurement, the twin Rh nanoparticles show little agglomeration while the chemical state remains unchanged (Supplementary Fig. 37, 38).

To further disclose the origin of high activity of Cs₃Rh₂I₉/NC-R in the alkaline HER process, the DFT calculation was performed. Based on the above characterizations, the Cs₃Rh₂I₉ clusters-derived Rh

nanoparticles possess larger lattice spacings and more GBs that liquid-reduced Rh nanoparticles and Rh particles from electro-reduction of bulk Cs₃Rh₂I₉. Thus, different Rh models with larger lattice spacings and more GBs were built to study the HER mechanism in alkaline. As shown in Supplementary Fig. 39, the increase of H-O-H angle and water molecule binding energy agrees well with the degree of distortion and crystal tension, indicating the enhanced ability of water

dissociation. Moreover, the largest H–O–H angle of 105.25° is found when water molecule is adsorbed on GBs with low coordination number, which further shows GBs would activate the H–OH bond. The water disassociation, as a pre-reaction to form an adsorbed proton, plays a more critical role in alkaline hydrogen evolution^{8,42}. The linear Brønsted–Evans–Polanyi relationship between adsorption energy and dissociative kinetic barrier of H₂O allows the use of binding energy of water molecule as the activity descriptor for alkaline HER. The sites at GBs and tensed Rh atoms show high H₂O binding energy. The enhanced water dissociation ability in Cs₃Rh₂I₉/NC-R was further verified by in situ Raman spectra. Supplementary Fig. 40a shows obvious interfacial water on Cs₃Rh₂I₉/NC-R surface in 1 M KOH solution over the potential range from 0 to –0.3 V (vs. RHE). The peaks at 1588 and 1632 cm^{–1} correspond to the G band of carbon substrate and the adsorbed water on Rh, respectively^{43,44}. As the potential decreased, the intensity of H–O–H bending increases sharply. However, such a phenomenon is absent in Rh/NC synthesized by chemical reduction (Supplementary Fig. 40b). Thus, the abundant and multiply active sites on twin crystal Rh are effective for cleaving the H–OH bond, contributing to the high electrochemical performance toward HER under alkaline condition.

Discussion

The defects-rich Rh nanoparticles with average size of ~2.2 nm were prepared by in situ electrochemical reduction of perovskite Cs₃Rh₂I₉ cluster via a bottom-up evolution route. The reduction was investigated by in situ EQCM, ex-situ ICP-MS, and XPS. The as-formed twin crystal Rh nanoparticles with tensile stress exhibits excellent activity and stability in alkaline hydrogen evolution reaction. In 1.0 M KOH, the Cs₃Rh₂I₉/NC-R catalyst showed a low overpotential of 25 mV at the current density of 10 mA cm^{–2} and a small Tafel slope of 30.3 mV dec^{–1}. Cs₃Rh₂I₉/NC-R exhibits high mass activity of 839.8 mA mg^{–1}_{Rh}, 21.6 times that of Cs₃Rh₂I₉-R with bigger size and 2.4 times that of liquid-reduced Rh/NC. In a chlor-alkali electrolyte, the area activity of Cs₃Rh₂I₉/NC-R (0.067 mA cm^{–2}_{ECSA} at –50 mV vs. RHE) manifests a factor of 4.1 and 2.0 activity increase compared to Cs₃Rh₂I₉-R and Rh/NC, respectively. Moreover, it exhibits good durability with negligible activity loss for 50 h HER measurement. The DFT calculation revealed that Rh nanoparticles of Cs₃Rh₂I₉/NC-R enriched with multiply catalytic sites could accelerate the activation of adsorbed water molecule, thereby smoothing the whole alkaline HER. The study presents new insights into preparing small-sized nanoparticles via in situ electrochemical reconstruction for energy electrocatalysis.

Methods

Synthesis of Cs₃Rh₂I₉ crystal

The Cs₃Rh₂I₉ crystal was prepared *via* solid state reaction. 50 mg rhodium, 185 mg iodine and 1.5 g CsI were mixed by grinding in Ar glovebox to prevent the influence of water. CsI was served as both raw material and flux. The above powder was annealed at 800 °C for 2000 min in the evacuated quartz tube and cooled to room temperature at the rate of 3 °C min^{–1}. Finally, the product was washed with deionized water for several times and dried in vacuum at room temperature.

Synthesis of NC

NC was prepared by the sol–gel method according to our previous report.⁴¹ It started from mixing 1.8 mL formaldehyde and 1 g melamine in 20 mL deionized water under stirring at 50 °C for 1 h. Then, 4.5 g MnCl₂ and 6 g PEG were added into the above solution and continuously stirred at room temperature to form a uniform sol. The sol was transferred into a culture dish and dried at 80 °C for 24 h to form a gel precursor. The gel was cut into small slices and pre-carbonized at 400 °C for 2 h in an Ar atmosphere. After grounding the precursor into powder, it was annealed at 900 °C with a heat rate of 3 °C min^{–1} in the

Ar atmosphere. The final product NC was obtained by acid treatment to remove the metal impurities.

Synthesis of nanoclusters Cs₃Rh₂I₉ supported on NC (Cs₃Rh₂I₉/NC)

10 mg Cs₃Rh₂I₉ crystal was added into 40 mL *N,N*-dimethylformamide (DMF) and stirred at 60 °C to form the brown solution. Then, 10 mg NC was added and the mixture was continually stirred for 1 h. Subsequently, the above mixture was slowly added into 200 mL H₂O under fiercely stirring. The induced polar protic solvent with slow S_N2 reaction kinetics results in the precipitation of Cs₃Rh₂I₉⁴⁵. The Cs₃Rh₂I₉/NC was collected by suction filtration and washed by water and ethanol for several times. And it was dried in vacuum at 60 °C for 12 h. Cs₃Rh₂I₉/NC with different Rh contents (*x* wt.%, *x* = 2.7, 4.3, 5.8, or 7.1) was prepared by changing mass loading of Cs₃Rh₂I₉, and *x* corresponds to the Rh content. The optimized Cs₃Rh₂I₉/NC (5.8 wt.%) is named as Cs₃Rh₂I₉/NC in the main text and SI if no specific note was mentioned. The re-precipitated Cs₃Rh₂I₉ without adding NC was obtained as the control sample.

Synthesis of Rh/NC by liquid reduction

RhCl₃ (7.1 mg) was dissolved in 20 mL *N*-methyl pyrrolidone (NMP), followed by the addition of 46.5 mg NC. After stirring for 1 h, 0.05 g sodium borohydride in NMP was added into the above solution drop by drop. After stirring for 20 h, Rh/NC was collected by suction filtration and then annealed in 10% H₂/Ar at 300 °C for 30 min. The elemental analysis shows the mass content of Rh in Rh/NC is 7.0 wt.%.

Characterization

Single-crystal XRD data was obtained on a Bruker D8 QUEST diffractometer with Mo-*K*_α (λ = 0.71073 Å) radiation at 300 K. The crystal structure was solved and refined using APEX3 program. Powder XRD was performed on a Bruker D8 Advance diffractometer equipped with mirror-monochromatized source of Cu *K*_α radiation (λ = 0.15406 nm). The ultraviolet–visible (UV–Vis) light diffuse-reflectance spectra were measured on a UV-4100 spectrophotometer operating from 2000 to 300 nm at room temperature and the BaSO₄ powder was used as a 100% reflectance standard. Low-temperature electrical resistivity was measured using a Physical Properties Measurements System (PPMS-Dyna Cool, Quantum Design). SEM was conducted on the JSM-7800F. TEM was conducted on the JEM-2100F and Talos F200X G2. HAADF-STEM and EELS measurements were obtained from aberration-corrected TEM (Hitachi HF5000) and JEOL Triple-C TEM. The chemical states were investigated by X-ray photoelectron spectroscopy (XPS, Thermo Fisher Scientific ESCA Lab 250Xi spectrometer) with focused monochromatic Al *K*_α radiation (1486.6 eV, 150 W; 500 μm diameter of irradiated area). Ion concentration in electrolyte was determined by the inductively coupled plasma mass spectrometry (XII, Thermo Fisher Scientific). X-ray absorption fine-structure spectroscopy (XAFS) was performed at the Materials Research Collaborative Access Team (MRCAT), Sector 10-BM line at the Advanced Photon Source at Argonne National Laboratory⁴⁶. Data were processed and fitted using Athena and Artemis for the IFEFIT suite^{47,48}. All spectra were prepared for Fourier Transform using a Hanning window ranging from 2.0 Å^{–2} < *k* < 14 Å^{–1} with *dk* = 2 Å^{–1} and simultaneously fitted in *k*, *k*², and *k*³ weightings using a Hanning window of 1.8 Å < *R* < 2.8 Å with *dR* = 0.2 Å. Wavelet transforms were obtained from processed data using Larch⁴⁹.

Hydrogen evolution reaction experiments

The electrochemical performance was conducted on the three-electrode system using graphite rod as counter electrode and Hg/HgO as the reference electrode at 25 °C. 5 mg catalyst and 25 μL Nafion (5 wt.%) were added into 475 μL ethanol to form the homogeneous catalyst ink. And the working electrode was prepared by adding 15 μL

ink on a rotating GCE (area: 0.1963 cm²). The catalyst loading amount on GCE is 0.764 mg cm⁻². And the calculated Rh loading amounts on GCE are 0.045, 0.090, and 0.053 mg cm⁻² for Cs₃Rh₂I₉/NC-R, Cs₃Rh₂I₉-R, and Rh/NC, respectively. Moreover, the commercial Pt/C (Pt content: 20 wt.%) was also used as the control electrocatalyst. The HER measurements were performed in the Ar-saturated electrolyte at the rotating speed of 1600 rpm. Before measurement, the electrode was activated (reduced) under the CV between 0.075 and -0.175 vs. RHE at a scan rate of 100 mV s⁻¹ for 100 cycles. The linear sweep voltammetry (LSV) curves were recorded at the scan rate of 5 mV s⁻¹ with the IR-compensation 90%. The ECSA was obtained from the equation $ECSA = C_{dl}/C_s$, where the electrochemical double layer capacitance (C_{dl}) was obtained from the CV measurement at different scan rates and the specific capacitance (C_s) was 0.4 μF cm⁻² in 1.0 M KOH. In chlorine-alkali electrolyte (3.0 M NaOH + 3.0 M NaCl), the Hg/HgO electrode was protected by the salt bridge (1.0 M KOH).

The durable measurement was conducted in a two-compartment cell using the cation exchange membrane as the separator. And the working electrode was prepared by dropping the ink on the carbon cloth (catalyst loading amount: 1 mg cm⁻²).

Reversible hydrogen electrode (RHE) calibration

The calibration was performed in the H₂-saturated electrolyte using Pt foils as counter electrode and working electrode. CV measurements were carried out at the scan rate of 1 mV s⁻¹. The average potentials at the current of zero were set as the thermodynamic potential of RHE.

Electrochemical quartz crystal microbalance experiment

The EQCM experiment was conducted on the QSense Explorer instrument (Biolin Scientific AB, Sweden). The working electrode was prepared by spin-coating the catalyst ink on the Au-coated quartz crystal disk (5 MHz). In situ EQCM was measured simultaneously with potentiostatic measurement at -0.03 V vs. RHE.

Hydrogen production faradic efficiency

The faradic efficiency was determined by the drainage method at 25 °C. A constant current was applied on the electrode, and the electrocatalysis time and the volume of evolved hydrogen were recorded synchronously. Each experiment was repeated three times. The experimental content of produced hydrogen was calculated by the Ideal Gas Law and the theoretical content was determined by the Faraday Law.

Computational methods

All theoretical calculations were performed using DFT, as is implemented in the Vienna ab initio simulation package (VASP). The electron exchange and correlation energy functionals are treated using the generalized gradient approximation, as is captured using the Perdew-Burke-Ernzerh functional (GGA-PBE). Iterative solutions of the Kohn-Sham equations were done using a plane-wave basis set defined using a kinetic energy cutoff of 500 eV. The k-point sampling was obtained from the Monkhorst-Pack scheme with a (6 × 6 × 1) mesh, respectively. Rh (001) surface structures with lattice tensile of 1.5% and 3% were built and optimized to simulate active sites with different crystal strain. Surface structures with Rh (110) GB and standard Rh (001) were chosen to reflect the properties of GB and monocrystal Rh, respectively. Water bonding energy (ΔE_{H_2O}) was calculated by the following equation:

$$\Delta E_{H_2O} = E_{H_2O} + E_{sub} - E_{total}$$

whereas E_{total} refers to energy of substrate with corresponding adsorbate, ΔE_{H_2O} refer to energy of one H₂O molecule, T is selected by room temperature (298 K), and ZPE refers to zero point energy.

Data availability

All data generated or analyzed during this study are included in this published article and its supplementary information file. Source data are provided with this paper.

References

- Oener, S. Z., Foster, M. J. & Boettcher, S. W. Accelerating water dissociation in bipolar membranes and for electrocatalysis. *Science* **369**, 1099–1103 (2020).
- Zhu, J. Q. et al. Boundary activated hydrogen evolution reaction on monolayer MoS₂. *Nat. Commun.* **10**, 1348 (2019).
- McCrum, I. T. & Koper, M. T. M. The role of adsorbed hydroxide in hydrogen evolution reaction kinetics on modified platinum. *Nat. Energy* **5**, 891–899 (2020).
- Hu, C., Zhang, L. & Gong, J. Recent progress made in the mechanism comprehension and design of electrocatalysts for alkaline water splitting. *Energy Environ. Sci.* **12**, 2620–2645 (2019).
- Peugeot, A. et al. Benchmarking of oxygen evolution catalysts on porous nickel supports. *Joule* **5**, 1281–1300 (2021).
- Li, Y. P. et al. Partially exposed RuP₂ surface in hybrid structure endows its bifunctionality for hydrazine oxidation and hydrogen evolution catalysis. *Sci. Adv.* **6**, eabb4197 (2020).
- Subbaraman, R. et al. Enhancing hydrogen evolution activity in water splitting by tailoring Li-Ni(OH)(2)-Pt interfaces. *Science* **334**, 1256–1260 (2011).
- Ju, Q. J. et al. Ruthenium triazine composite: a good match for increasing hydrogen evolution activity through contact electrification. *Adv. Energy Mater.* **10**, 2000067 (2020).
- Lu, K. et al. Li_xNiO/Ni heterostructure with strong basic lattice oxygen enables electrocatalytic hydrogen evolution with Pt-like Activity. *J. Am. Chem. Soc.* **142**, 12613–12619 (2020).
- Lin, Z. P. et al. Realizing negatively charged metal atoms through controllable d-electron transfer in ternary Ir_{1-x}Rh_xSb intermetallic alloy for hydrogen evolution reaction. *Adv. Energy Mater.* **12**, 2200855 (2022).
- Li, S. L. et al. Geometric structure and electronic polarization synergistically boost hydrogen-evolution kinetics in alkaline medium. *J. Phys. Chem. Lett.* **11**, 3436–3442 (2020).
- Li, Z. C. et al. Spin engineering of single-site metal catalysts. *Innovation* **3**, 100268 (2022).
- Lin, G. X. et al. Caged-cation-induced lattice distortion in bronze TiO₂ for cohering nanoparticle hydrogen evolution electrocatalysts. *ACS Nano* **16**, 9920–9928 (2022).
- Liu, Y., Xiao, C., Huang, P., Cheng, M. & Xie, Y. Regulating the charge and spin ordering of two-dimensional ultrathin solids for electrocatalytic water splitting. *Chem* **4**, 1263–1283 (2018).
- Yan, Y., Xia, B. Y., Zhao, B. & Wang, X. A review on noble-metal-free bifunctional heterogeneous catalysts for overall electrochemical water splitting. *J. Mater. Chem. A* **4**, 17587–17603 (2016).
- Feng, G. et al. Sub-2 nm ultrasmall high-entropy alloy nanoparticles for extremely superior electrocatalytic hydrogen evolution. *J. Am. Chem. Soc.* **41**, 17117–17127 (2021).
- Huang, Y. et al. Atomically engineering activation sites onto metallic 1T-MoS₂ catalysts for enhanced electrochemical hydrogen evolution. *Nat. Commun.* **10**, 982 (2019).
- Xu, C. et al. Facile synthesis of effective Ru nanoparticles on carbon by adsorption-low temperature pyrolysis strategy for hydrogen evolution. *J. Mater. Chem. A* **6**, 14380–14386 (2018).
- Zhang, J. et al. Single platinum atoms immobilized on an MXene as an efficient catalyst for the hydrogen evolution reaction. *Nat. Catal.* **1**, 985–992 (2018).
- Shen, S. J. et al. Highly active Si sites enabled by negative valent Ru for electrocatalytic hydrogen evolution in LaRuSi. *Angew. Chem. Int. Ed.* **61**, e202206460 (2022).

21. Deng, J. F., Chen, S. P., W, X. J., Zheng, J. & Li, X. G. Recent progress on materials for hydrogen generation via hydrolysis. *J. Inorg. Mater.* **36**, 1–8 (2020).
22. Kuai, C. G. et al. Phase segregation reversibility in mixed-metal hydroxide water oxidation catalysts. *Nat. Catal.* **3**, 743–753 (2020).
23. Weng, Z. et al. Metal/oxide interface nanostructures generated by surface segregation for electrocatalysis. *Nano Lett.* **15**, 7704–7710 (2015).
24. Liao, H., Fisher, A. & Xu, Z. J. Surface segregation in bimetallic nanoparticles: a critical issue in electrocatalyst engineering. *Small* **11**, 3221–3246 (2015).
25. Gong, S., Zhang, Y.-X. & Niu, Z. Recent advances in earth-abundant core/noble-metal shell nanoparticles for electrocatalysis. *ACS Catal.* **10**, 10886–10904 (2020).
26. Du, W., Shi, Y. M., Zhou, W., Yu, Y. F. & Zhang, B. Unveiling the in situ dissolution and polymerization of Mo in Ni₄Mo alloy for promoting the hydrogen evolution reaction. *Angew. Chem. Int. Ed.* **60**, 7051–7055 (2021).
27. Escalera-López, D. et al. Phase- and surface composition-dependent electrochemical stability of Ir-Ru nanoparticles during oxygen evolution reaction. *ACS Catal.* **11**, 9300–9316 (2021).
28. Dutta, A., Samantara, A. K., Dutta, S. K., Jena, B. K. & Pradhan, N. Surface-oxidized dicobalt phosphide nanoneedles as a non-precious, durable, and efficient OER catalyst. *ACS Energy Lett.* **1**, 169–174 (2016).
29. Li, S. L. et al. A glass-ceramic with accelerated surface reconstruction toward the efficient oxygen evolution reaction. *Angew. Chem. Int. Ed.* **133**, 3817–3824 (2020).
30. Zeng, Y. et al. Surface reconstruction of water splitting electrocatalysts. *Adv. Energy Mater.* **12**, 2201713 (2022).
31. Liu, X. et al. Comprehensive understandings into complete reconstruction of precatalysts: synthesis, applications, and characterizations. *Adv. Mater.* **33**, 2007344 (2021).
32. Jiang, H., He, Q., Zhang, Y. & Song, L. Structural self-reconstruction of catalysts in electrocatalysis. *Acc. Chem. Res.* **51**, 2968–2977 (2018).
33. Zhang, Y. et al. Observation of a robust and active catalyst for hydrogen evolution under high current densities. *Nat. Commun.* **13**, 7784 (2022).
34. Stern, L.-A., Feng, L., Song, F. & Hu, X. Ni₂P as a Janus catalyst for water splitting: the oxygen evolution activity of Ni₂P nanoparticles. *Energy Environ. Sci.* **8**, 2347–2351 (2015).
35. Yu, J. et al. Monoclinic SrIrO₃: an easily synthesized conductive perovskite oxide with outstanding performance for overall water splitting in alkaline solution. *Chem. Mater.* **32**, 4509–4517 (2020).
36. Zhao, S., Yang, Y. & Tang, Z. Insight into structural evolution, active sites, and stability of heterogeneous electrocatalysts. *Angew. Chem. Int. Ed.* **61**, e202110186 (2022).
37. Aoki, Y. et al. In situ activation of a manganese perovskite oxygen reduction catalyst in concentrated alkaline media. *J. Am. Chem. Soc.* **143**, 6505–6515 (2021).
38. Gao, L., Cui, X., Sewell, C. D., Li, J. & Lin, Z. Recent advances in activating surface reconstruction for the high-efficiency oxygen evolution reaction. *Chem. Soc. Rev.* **50**, 8428–8469 (2021).
39. McCall, K. M. et al. From OD Cs₃Bi₂I₉ to 2D Cs₃Bi₂I₆Cl₃: dimensional expansion induces a direct band gap but enhances electron–phonon coupling. *Chem. Mater.* **31**, 2644–2650 (2019).
40. Kortüm, G., Braun, W. & Herzog, G. Principles and techniques of diffuse-reflectance spectroscopy. *Angew. Chem. Int. Ed.* **2**, 333–341 (1963).
41. Lin, G. et al. Suppressing dissolution of Pt-based electrocatalysts through the electronic metal–support interaction. *Adv. Energy Mater.* **11**, 2101050 (2021).
42. Yang, G. C. et al. Interfacial engineering of MoO₂-FeP heterojunction for highly efficient hydrogen evolution coupled with biomass electrooxidation. *Adv. Mater.* **32**, e2000455 (2020).
43. Senior, W. A. et al. Assignment of the infra-red and Raman bands of liquid water. *Nature* **205**, 170 (1965).
44. Ren, B. et al. Surface Raman spectra of pyridine and hydrogen on bare platinum and nickel electrodes. *J. Electroanal. Chem.* **415**, 175–178 (1996).
45. Kim, B. J. et al. Selective dissolution of halide perovskites as a step towards recycling solar cells. *Nat. Commun.* **7**, 11735 (2016).
46. Kropf, A. J. et al. The new MRCAT (Sector 10) bending magnet beamline at the advanced photon source. *AIP Conf. Proc.* **1234**, 299–302 (2010).
47. Ravel, B. & Newville, M. ATHENA, ARTEMIS, HEPHAESTUS: data analysis for X-ray absorption spectroscopy using IFFEFIT. *J. Synchrotron Radiat.* **12**, 537–541 (2005).
48. Newville, M. IFFEFIT: interactive XAFS analysis and FEFF fitting. *J. Synchrotron Radiat.* **8**, 322–324 (2001).
49. Newville, M. Larch: an analysis package for XAFS and related spectroscopies. *J. Phys.: Conf. Seri.* **430**, 012007 (2013).

Acknowledgements

The authors are grateful to the financial support from the National Natural Science Foundation of China (92163117 for J.W., 52072389 for J.W.), Science and Technology Commission of Shanghai Municipality (22DZ1205600 for J.W., 20520760900 for J.W., 21ZR1473300 for W.Z.), State Key Laboratory of ASIC & System (2020KF002 for J.W.) and Shanghai Science and Technology Innovation Action Plan (20DZ1204400 for F.H.). Analytical Instrumentation Center (No. SPSTAIC10112914), SPST, ShanghaiTech University. J.W. thanks the Program of Shanghai Academic Research Leader (20XD1424300) for financial support. MRCAT operations are supported by the Department of Energy and the MRCAT member institutions. This research used resources from the Advanced Photon Source, a U.S. Department of Energy (DOE) Office of Science User Facility operated for the DOE Office of Science by Argonne National Laboratory under Contract No. DE-AC02-06CH11357. Q.L. and K.S. thank the JST-CREST and ER-C MORE-TEM synergy projects.

Author contributions

G.L., Z.Z., and Q.J. contributed equally to this work. F.H. and J.W. supervised and led the project. G.L., Z.Z., and Y.M. performed materials synthesis. Q.J. conducted theoretical calculations. G.L. and T.W. characterized the materials. C.S. and W.C. helped with XAFS. H.P., H.Z., and Z.L. helped with XPS measurement. Q.L. and K.S. collected the atomic-scale STEM images of Rh nanoparticles. Y.Z. conducted EQCM experiment. G.L. and S.K. carried out electrochemical experiments. G.L. wrote the manuscript. W.Z., F.H., and J.W. revised the manuscript.

Competing interests

The authors declare no competing interests.

Additional information

Supplementary information The online version contains supplementary material available at <https://doi.org/10.1038/s41467-023-35783-y>.

Correspondence and requests for materials should be addressed to Fuqiang Huang or Jiacheng Wang.

Peer review information *Nature Communications* thanks the other anonymous reviewer(s) for their contribution to the peer review of this work. Peer review reports are available.

Reprints and permissions information is available at <http://www.nature.com/reprints>

Publisher's note Springer Nature remains neutral with regard to jurisdictional claims in published maps and institutional affiliations.

Open Access This article is licensed under a Creative Commons Attribution 4.0 International License, which permits use, sharing, adaptation, distribution and reproduction in any medium or format, as long as you give appropriate credit to the original author(s) and the source, provide a link to the Creative Commons license, and indicate if changes were made. The images or other third party material in this article are included in the article's Creative Commons license, unless indicated otherwise in a credit line to the material. If material is not included in the article's Creative Commons license and your intended use is not permitted by statutory regulation or exceeds the permitted use, you will need to obtain permission directly from the copyright holder. To view a copy of this license, visit <http://creativecommons.org/licenses/by/4.0/>.

© The Author(s) 2023